Impact mechanics of multilayer composite armors: Analytical modeling, FEM numerical simulation, and ballistic experiments

Stefano Signetti[a,1,*], Seunghwa Ryu[b], Nicola M. Pugno[a,c,**]

a: Laboratory of Bioinspired, Bionic, Nano, Meta Materials & Mechanics, Department of Civil, Environmental and Mechanical Engineering, University of Trento, via Mesiano 77, I-38123 Trento, Italy

b: Department of Mechanical Engineering, Korea Advanced Institute of Science and Technology (KAIST), 291 Daehak-ro, Yuseong-gu, Daejeon 34141, Republic of Korea c School of Engineering and Materials Science, Queen Mary University of London, Mile End Road, London E1 4NS, United Kingdom

c: School of Engineering and Materials Science, Queen Mary University of London, Mile End Road, London E1 4NS, United Kingdom

∗ Corresponding author.

∗∗ Corresponding author at: Laboratory of Bioinspired, Bionic, Nano, Meta Materials & Mechanics, Department of Civil, Environmental and Mechanical Engineering, University of Trento, via Mesiano 77, I-38123 Trento, Italy.

E-mail addresses: stefano.signetti@ex-staff.unitn.it (S. Signetti), nicola.pugno@unitn.it (N.M. Pugno).

1 Currently at: Fraunhofer-Institute for High-Speed Dynamics, Ernst-Mach-Institut, EMI, Ernst-Zermelo-Str. 4, 79104 Freiburg im Breisgau, Germany

Keywords: High-velocity impact, Ballistic tests, Composite armors, Finite element simulations, Fracture mechanics

Abstract

An analytical model is developed to study the ballistic behavior of multilayer composite armors subjected to the high-velocity impact of projectiles with arbitrary angle of incidence, shape, size, and frictional characteristics. The thickness compaction resulting from the production process is also accounted for, quantifying the role of the curing pressure on the enhancement of the impact toughness of composite laminates. Finite element method simulations are used in a complementary manner to study damage and failure mechanisms within the targets. Both approaches are validated by extensive experimental ballistic tests on multilayer composite targets. The role of the layer stacking sequence is also investigated. It emerges that graded multilayer configurations yield higher toughness when the projectile penetrates plies with decreasing fracture strength. These results can explain common structural arrangements in biological armors as well as be exploited in the design and optimization of shielding structures against high-velocity projectiles

1. Introduction

One of the main challenges in the technology of protective armors, is the achievement of the highest protection levels –as defined by related standards [1]– against high-velocity penetrators even when a massive system, either in terms of size and weight, is neither desired nor suitable for the specific application. For example, lightweight shields are fundamental to ensure an efficient mobility to terrestrial vehicles, aircrafts, and spacecrafts [2] while mechanical flexibility is desired to guarantee ergonomics in body armors for defense or sports applications [3].

Body armors are generally manufactured with fiber–matrix composites [4] due to their lightness and good ballistic protection in terms of kinetic energy dissipation per unit mass. They are generally formed by assembling layers of unidirectional (UD) or woven fabrics made of highperformance fibers embedded in a thermosetting resin, which holds the desired shape to the armor [5]. These high-strength fibers include the families of para-aramid (Kevlar®, Twaron®, Technora®), highperformance polyethylene (Spectra®, Dyneema®) and, more recently, ®
Polybenzoxaloze (Zylon). All the above fibers are characterized by a high tensile modulus over density ratio and specific toughness [6,7]. Composites are also acknowledged to possess good corrosion resistance [8], damage tolerance [8,9], and fatigue properties [10] with respect to traditional armors materials, such as metal alloys. Another important characteristic is the limited degradation of properties after multiple impact events, which guarantees the long-term survivability of the protective systems in harsh environments [11]. In order to protect against high-velocity and penetrating masses (e.g., armor piercing projectiles) a hard-face ceramic layer can be introduced in order to first damage and shatter the projectile [12,13], while the residual kinetic energy is dissipated through the deformation of the backing multilayer composite package [14,15]. This solution can be considered, to some extent, bio-inspired as it can be found in many examples of natural dermal armors, evolved to protect against the bite of predators, which are composed by an external hard mineral layer and a fibrous multilayer collagen substrate [16–18].

Experimental testing has represented for a long time the most straightforward method for achieving required levels of performance, but it is generally costly, time-consuming, and often not sufficient
for obtaining a significant amount of data, as well as in a systematic form, for optimization. Numerical simulations are relatively cost- and time-effective, but require a relatively high computing power and resources depending on the level of detail. They may also present some intrinsic limits, especially when dealing with multiphysics and multiscale phenomena. Analytical methods are an important alternative whenever closed-form mathematical equations can be set up to describe the dominant physical phenomena that occur during the impact event, as long as the assumptions inherent in the model are applicable. Several studies about the analytical modeling of ballistic impact of multilayer fabric panels [19–26], based either on energy or momentum balance, are available in the literature.

While fiber mechanical properties are important, the structural assembly plays a key role in determining the ballistic protection performance of multilayer armors. For example, the orientation and the geometry of the yarns can significantly change the constitutive response of the ply [7]. The importance of compaction in the curing process for the final performance of laminates is also widely acknowledged in the industry. For example, Hubert and Pousartip [27] experimentally investigated the role of the textile orientation, of the component geometry and of their interaction on the resin flow in the mold in determining the final quality of the composite. However, a comprehensive and consistent theory for explaining and quantifying the role of hot pressing on the improvement of impact performances has hitherto to be reported and included in related models. Indeed, the increase in the fiber volume fraction, due to resin flow and leak outside the mold, may not be able alone to explain the scaling of impact properties [7,12,28].

Nowadays, non-linear finite element method (FEM) approaches are capable of modeling the primary mechanical phenomena that occur in high-velocity impact events such as contact, inter-layer delamination, material constitutive response, fracture and fragmentation [11], making possible the accurate replication of ballistic tests and their partial substitution in the design and optimization process [12,29–31]. Such codes include sophisticated constitutive models, also accounting

for strain-rate effects and anisotropic failure criteria, which enable the modeling of the most complex materials and structural configurations. In this regard, the accuracy and prediction capabilities in the design process of such models primarily rely on the accurate characterization of the mechanical properties at the laminate and sub-laminate levels [7].

In this paper we propose an analytical model and a FEM simulation framework to study the ballistic performance of multilayer composite armors subjected to the impact of high-velocity penetrators (300–800m⁄s). The aim is to study the effects of both material and structural assemblies on the scaling of the protection capability, towards optimized solutions. Acknowledged penetration models based on conservation of momentum are here extended to multilayer and heterogeneous targets. The effect of thickness reduction by pressure compaction is included in the model by scaling the failure strength of the laminate materials according to Linear Elastic Fracture Mechanics (LEFM); this interpretation is further confirmed by quantitative experimental comparison via a fractal energy dissipation approach. The role of the layers stacking sequence, in terms of materials strength distribution through the thickness, is also investigated. Analytical and numerical results are extensively validated against experimental data from ballistic tests, showing very good prediction capabilities in terms of impact toughness, deformation, and damage upon several impact scenarios, including heterogeneous targets and oblique collisions.

2. Methods

2.1. Analytical impact model

The variables considered in the penetration model are: the geometry of the target (the number of layers and their stacking sequence and thickness), the materials properties (failure strength and its strain-rate dependence, and density), the projectile impact characteristics (mass, velocity, and obliquity) and geometry (diameter and profile).

Dissipation of energy via inter-layer delamination is neglected, since marginal if compared to other mechanisms. Energy partitioning into heat, either due to deviatoric or volumetric compression, is not accounted for in this model. Indeed, in the regime of interest thermal effects are generally considered negligible [32], as later confirmed by results. Parallel, some experiments would confirm that this assumption is reasonable up to 700–800m⁄s, when melting may start to occur for the thermoset resin or PE fibers [33].

Assuming the conservation of momentum according to Newton's second law of motion, the reduction of the instantaneous velocity v of a projectile penetrating a bulk target can be computed, by integrating the following differential equation, if an expression of the net resisting force F acting on the projectile of mass m is known: $\frac{dv}{dt}\frac{dv}{dh}$

$$m\dot{v} = mv\frac{dv}{dh} = -F, \quad (1)$$

where h is the instantaneous depth of penetration of the projectile in the target. Considering the dissipation of the projectile kinetic energy in a volume of target material defined by the projectile imprint radius r and by the laminate thickness t, F can be assumed as a first approximation to be constant and equal to $\sigma\pi r^2$, where σ is the material fracture strength. This means that the relation between the residual projectile kinetic energy (K_{res}) and its initial impact value (K_0) is linear, with unitary slope and intercept Ft [12]. This result is far from the reality, being the slope generally lower than the unity, due to additional dissipation, such as projectile deformation and the generation of ejecta. Moreover, by assuming a constant expression for F strain-rate effects are not taken into account and the material strength is assumed to be equal to its nominal static value. To include rate-dependence, the armor material strength can be written as a quadratic form of the current impact velocity v [34]:

$$\sigma = \sigma_0\left[a_0 + \frac{1}{\left(\frac{V}{v}\right)}\left(a + a_2\left(\frac{v}{V}\right)^2\right)\right], \quad (2)$$

where $V = \sqrt{\sigma_0/\rho_0}$ [35] is a characteristic velocity, which is a function of the static fracture strength of the material σ_0 and of its density ρ_0 in the undeformed state. The dimensionless coefficients a_0, a_1, and a_2 modify the plate strength taking into account the projectile shape effects [36]:

$$a_0 = A_0\left(1 + r_2\sqrt{f_0}\right), \quad (3a)$$

$$a_1 = A_1\left(1 - r_2\sqrt{f_1}\right), \quad (3b)$$

$$a_2 = A_2\left(1 - {}_2f_2\frac{}{r}\right) \quad (3c)$$

where A_0, A_1, and A_2 are dimensionless coefficient experimentally determined for different constitutive models [35,37], which can be obtained from the best fit of ballistic curves from perforation experiments. The quantities f_0, f_1 and f_2 are shape functions, which depend on the impactor geometry. Defining the projectile profile with a function $y(x)$, we have [36]:

$$f_0 = \mu\int_h y\,dx, \quad (4a)$$

$$f_1 = \int_h yy_x\left[1 - \frac{y_x + \mu}{\sqrt{1 + y_x^2}}\right]dx \quad (4b)$$

$$f^2{}_h = \int_h yy_x\left[1 - \frac{y_x + \mu}{\sqrt{1 + y_x^2}}\right]dx, \quad (4c)$$

where y_x is the derivative of the profile function along the axial direction of the projectile (x), μ is the dynamic friction coefficient between the impactor and the target, and h is the line integration domain corresponding to the instantaneous depth of penetration in

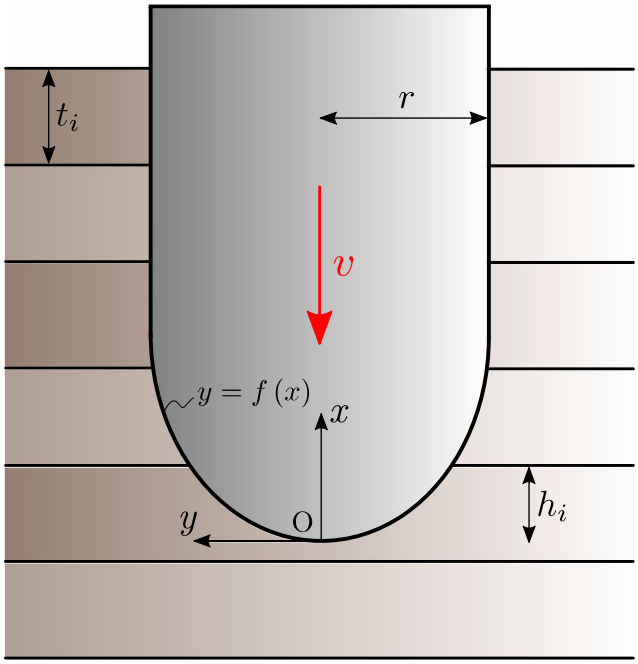

Fig. 1. Notation of geometrical quantities in the analytical model. y is the function describing the projectile shape as a function of the axial coordinate x. h_i is the current depth of penetration of the projectile in the i-th layer.

the material (Fig. 1). Thus, with Eqs. (4) it is possible to take into account the role of different projectile size, shape, and friction on the penetration capability for a given initial impact kinetic energy. Note that for $r \to \infty$ the shape effect given by Eqs. (3) vanishes and that, when $a_1 = a_2 = 0$, $\sigma = \sigma_0 a_0$ represents the nominal static strength corrected by the projectile shape factor.

Let consider now a multilayer target made of a stacking of N layers of arbitrary thicknesses t_i and different incompressible elasticperfectly plastic, homogeneous and isotropic materials, each of them with strength σ_i. We define as V_i the exiting velocity of the projectile after its passage through the i-th layer. Eq. (1) applied to a single layer of the laminate becomes:

$$\int_{V_{i-1}}^{V_i} mv\,dv = -\int_0^{t_i} F_i\,dh. \tag{5}$$

By introducing the strain-rate dependence in the considered expression of F, according to Eq. (2), we have: $V_i t_i$(v) (v)2]

$$\int_{V_{i-1}}^{V_i} mv\,dv = -\int_0^{t_i} \sigma_{0,i}\pi r^2 \left[a_{0,i} + a_{1,i}\frac{v}{V_i} + a_{2,i}\frac{v}{V_i}\right] dh, \tag{6}$$

and then

$$\int_{V_{i-1}}^{V_i} \frac{mv}{\sigma_{0,i}\pi r^2 \left[a_{0,i} + a_{1,i}\left(v/V_i\right) + a_{2,i}\left(v/V_i\right)^2\right]}\,dv = -\int_0^{t_i} dh. \tag{7}$$

Note that, in this model, the laminate materials are then approximated as homogeneous and isotropic, with material properties (strength σ_0 and density) derived as for a rule of mixture from those of single constituents [7]. Through the solution of the integral of Eq. (7) it is possible to find the residual velocity V_i of the impactor after the penetration of the i-th layer. When $V_i = 0$ it is possible to determine the final depth of penetration H, by summation, as:

$$H = \sum_{n=1}^{i-1} t_n + \int_0^{V_{i-1}} \frac{m\,v}{\sigma_{0,i}\pi r^2 \left[a_{0,i} + a_{1,i}\,v/V_i + a_{2,i}\,v/V_i^2\right]}\,dv \tag{8}$$

The integral appearing in the Eqs. (7) and (8) is not trivial. In order to obtain a closed-form solution we assume that $a_{1,i} = 0$, according to the acknowledged Poncelet approximation [36,37] and consistently with experimental observation in the literature [38]. Accordingly, Eq. (7) can be rewritten, after some operations, as: ( )

$$\int \frac{mV_{i-1}\,dV_i}{2a_{2,i}\pi r^2 V_{i-1}\left[a_{0,i}+a_{2,i}(V_i/V_{i-1})^2\right]} = -\int dh. \quad (9)$$

At this point, being the argument of the integral at the left-hand side the derivative of a logarithmic function, the velocity V_i of the projectile after the passage of the i-th layer can be explicated as a function of the residual velocity V_{i-1} after the perforation of the overhead layer:

$$V_i = \sqrt{V_{i-1}^2 \left(\frac{2a_{2,i}\sigma_{0,i}\pi r^2}{m}\right)\left[\frac{1}{a_{0,i}+a_{2,i}(V_i/V_{i-1})^2}\right]}$$

$$V_i = a_{2,i}\exp\left(-t_i\sqrt{\frac{m}{2a_{0,i}+a_{2,i}V_i}}\right) - a_{0,i}. \quad (10)$$

The above expression is valid as far as the argument under the square root is positive or equal to zero. If this condition is not satisfied, it means that the projectile has been stopped at the penetration of the i-th layer and the corresponding final depth of penetration H can be calculated as follows, accordingly to Eq. (8):

$$H = \frac{mV_{i-1}^2}{2a_{2,i}\sigma_i\pi r}\ln\left[1+\frac{a_{2,i}(V_{i-1}/V_i)^2}{a_{0,i}}\right] + \sum_{n=1}^{i-1} t_n. \quad (11)$$

The obtained result is consistent, since higher penetrator's mass m or velocity V_0 would result in higher depth of penetration, while higher target strength σ and density, and imprint radius r yield lower H. Note that the above solutions, recursively applied for a series of layers, represent a generalization of classical penetration models to multilayer and heterogeneous targets with an arbitrary stacking configuration.

Considering the more general case of non-normal impact with arbitrary obliquity –or angle of incidence– β (yaw angle between the projectile axis and the velocity vector assumed to be zero), the projectile imprint nearly becomes elliptical of area $A = \pi c_i d_i$, with the semi-mayor and semi-minor axes given respectively by the following relations:

$$c_i = r\sec\beta + \sum_{n=1}^{i-1} t_n\tan\theta, \quad (12a)$$

$$d_i = r + \sum_{n=1}^{i-1} t_n\tan\theta, \quad (12b)$$

where c_i is the axis in the motion plane of the penetrator, d_i the one along its orthogonal direction, and θ is the angle of the damage cone through the thickness, which is about 45° for composite materials [12, 38]. Thus, the resisting force for the i-th layer becomes $F_i = \sigma_i\pi c_i d_i$ and, by posing $r_i = c_i d_i$ in Eq. (6), a further generalization of the model for oblique impacts is obtained. Thus, in this configuration, the capacity of the projectile to perforate the target is proportionally reduced with increasing impact incidence β. We highlight that the symmetry assumptions of this model represent a simplification with respect to the real scenario in terms of material orthotropy. Moreover, the shape of the perforation crater can assume more or less complex shapes depending on various factors, such as the material properties, layer stacking sequence, and impact velocity. The effects of such discrepancies could be incorporated in our model in the fitting parameters A_i (cf. Eqs. (3)).

Besides strain-rate effects (Eq. (2)), the ratios σ/ρ and E/ρ, respectively the specific material strength and stiffness, can be generally considered as material constants [39]. However, in the case of composites the situation is more complex. The thickness compaction resulting from the cleavage process would result in the reduction of number and size of defects at different dimensional scales, namely: surface, interface and volume porosity, macroscopic voids generated from complex geometries (e.g., at sharp corners), resin-rich areas, poor bridging at junctions, fibers/bundles rearrangement in the woven.

Let consider the compaction process during the cleavage and curing of woven textile-epoxy composites [27]. Assuming a compressible material, the lateral confinement implies $\rho \propto t^{-1}$ and, consequently, the characteristic fracture strength of the material is expected to scale similarly, namely $\sigma_{0,C} \propto t^{-1}$. However, under this assumption the role of defects, always present in materials and especially in fiber-reinforced composites, is neglected. The well-known energy approach proposed by Griffith [40] for the problem of a tensioned plate of unitary thickness with a pre-crack of length $2a$ yields the following LEFM relation of dependence between the characteristic material strength and the size of the characteristic crack:

$$\sigma_{0,C} = \sqrt{\frac{EG_C}{\pi a}}, \quad (13)$$

where G_C is the material fracture energy, and $K_C = \sqrt{EG_C}$ its fracture toughness. The characteristic crack half-length a is proportional to the minimum dimension of the body, which represents an upper limit to the size of defects. In our case, this limit is represented by the thickness t of the single ply (thus $a \propto t$). Recalling that $\rho \propto t^{-1}$, Eq. (13) yields the following scaling law:

$$\sigma_{0,C} \propto t^{-\frac{1}{2}} \quad \sigma_{0,C} \propto t^{-\frac{3}{2}} \quad \frac{\sigma}{\rho} \to \sigma, \quad (14)$$

which shows the beneficial effect of thickness reduction by compaction, e.g. by employing higher curing pressures, on the material fracture strength and, thus, on the armor toughness. Consequently, we introduce the scaling law of Eq. (14) in the analytical model by mean of the quantity $\eta = t/t_0$, here defined as *compaction*

factor, namely the ratio between the laminate thickness after compaction and the nominal thickness of the uncured material ($0 < \eta < 1$). The nominal strength σ_0 in Eq. (2) is then replaced by $\sigma_{0,C}$, which includes compaction effects:

$$\sigma_{0,C} = \sigma_0 \eta^{-\frac{2}{3}}, \tag{15}$$

where η has to be empirically correlated to some characteristic parameters of the production process, for example the cleavage pressure or temperature, or the volume of resin flown outside the mold. This correlation is beyond the scope of this paper.

2.2. Finite element simulations

The LS-DYNA® v971 R10.1 solver by Livermore Software Technology Corporation [41] was used in this study. The simulated targets are comprised of a circular plate (only one quarter is simulated due to the symmetry of the system, one half in case of oblique impact) with radius $R = 60$mm, which is sufficiently large to avoid edge effect. Plates are fully clamped at the boundary.

The 8-node solid-shell (also ''thick-shell'') element, developed by Liu et al. [42], based on the Reissner–Mindlin kinematic assumption is employed for the target. This element formulation (ELFORM=1 [41]) allows the implementation of laminate shell theories. Being also the thickness a geometrical quantity, unlike in the classical thin-shell formulations, another advantage of the thick-shell is the computation of deformation in the out of-plane dimension, making this element formulation particularly accurate for the treatment of the high compressive contact stresses generated in the plies by transverse impact [43]. A reduced single-point in-plane integration rule is adopted. Although higher order in-plane integration schemes, e.g. 2×2 Gauss quadrature, could be chosen, we opted for this formulation since low-order integration schemes are the most stable when elements become largely distorted, as may happen in high-velocity impact simulations. Since single-point quadrature is related to a reduction of the stiffness matrix, spurious zero-energy modes of deformation (also known as hourglass modes) may arise, as usually occurs under high concentrated pressures. A viscous-form hourglass control [44] is used in the simulations (LSDYNA hourglass type 3 [41]). We have verified that the artificial energy introduced to mitigate hourglassing is below 5% of the deformation energy at each simulation timestep, both for the whole model and separately for each of its deformable subparts (layers). One element through the thickness is used to model the single plies. The thickshell elements are sampled with 14 integration points (IPs) through the thickness of which the 6 innermost are associated to the core of woven textile, while the outermost (4+4) are attributed to the epoxy matrix, if present. MAT-58 (LAMINATED COMPOSITE FABRIC [41]) is used to simulate the fabric materials. This is a continuum damage model based on the Matzenmiller–Lubliner–Taylor theory [45], intended to describe the failure of woven fabrics and composite laminates also accounting for post-critical behavior in tension, compression, and shear. This material model has been chosen also for its compatibility with the adopted thick-shell formulation and extensive validation for this kind of problems in the literature. Detailed information and discussion about
the integration scheme and the characterization of parameters for the material model are given in the study of Ref. [7].

The time-step $\Delta\tau$ used for the integration of the solution is selected on the basis of the mesh size in order to correctly describe the elastic wave propagation through the medium. Being v_c the propagation velocity of the elastic wave in a 3D linear elastic isotropic and homogeneous material given by

$$v_c = \sqrt{\frac{E(1-\nu)}{\rho(1+\nu)(1-\nu)}}, \tag{16}$$

the minimum time-step is computed as:

$$\Delta\tau = \frac{l_c}{v_c}, \tag{17}$$

where l_c is the minimum characteristic edge size among all elements of the model. For the thick-shell element $l_c = V/A_c$, where V is the volume of the element, and A_c its larger surface (which minimizes $\Delta\tau$). Consequently, l_c generally corresponds to the element thickness. In order to be conservative for the solution stability the wave speed velocity is computed for all simulations considering the stiffer phase of the composite, that is the fiber fraction, which minimizes the timestep. The initial time-step is automatically adjusted during the simulations upon the deformation of the elements, which may reduce the current l_c with respect to the initial undeformed state. The convergence test with respect to the mesh size is shown in Figure S1 in the Supplementary Information for two exemplary cases, demonstrating the convergence for the used characteristic mesh size of 0.1mm.

The adhesive contact interaction between the different plies, obtained via the curing process, and related delamination are implemented via a stress-based segment-to-segment tiebreak-type contact (LS-DYNA Option 6 [41]). Considering a pair of adjacent nodes belonging to two neighboring layers, these are initially tied and the contact interface can sustain traction. A stress-based law is implemented to define the constitutive behavior of the adhesive interface, which fails when the following condition is satisfied [41]: $\left(\frac{s_\perp}{\sigma_\perp}\right)^2 + \left(\frac{s_\parallel}{\sigma_\parallel}\right)^2 \geq 1$, (18)

where $s_\perp$ and $s_\parallel$ are the current normal and tangential stresses between two (initially) welded interface nodes, while $\sigma_\perp$ and $\sigma_\parallel$ are their corresponding limit values, which, in general, are different, thus defining an elliptic domain. We have assumed, conventionally, $\sigma_\perp = 0.35$GPa and $\sigma_\parallel = 0.10$GPa for all simulations. Once the nodes separate the contact locally switches to a segment-to-segment penalty algorithm and the layers can mutually interact with friction. The kinetic friction law used in the contact model to compute the current friction coefficient μ, as a function of the static and dynamic values, μ_S and μ_D respectively, assumes the following typical velocity-weakening expression:

$$\mu = \mu_D + (\mu_S - \mu_D)e^{-\gamma|u|}, \tag{19}$$

which is a function of the relative velocity u of the sliding nodes, and γ is a decay constant. The same friction law applies for the contact between the projectile and the plies of the target. An eroding segmentto-segment contact is used between the projectile and the target layers ($\mu_S = 0.40$ and $\mu_S = 0.30$ [46]): in this case the SOFT=2 option [41] is activated to minimize interpenetration, given the high mismatch between the stiffnesses of the projectile and of the composite materials of the target. No further scaling of the contact stiffness was operated.

Fracture of the plies is implemented by mean of element erosion, which is based on the failure criterion for the specific material model (MAT-58 [45]): when the failure condition is reached at all the integration points, the element is deleted from the simulation, properly accounting for its energy components in the overall balance.

The total simulation time for all simulations is of 0.07ms, which ensures complete stop or penetration of the target with stabilization of the projectile residual velocity (V_{res}). More details about the caracterization of the material properties and on contact parameters used in the model can be found in Ref. [7].

2.3. Materials

In order to validate the developed analytical model and the FEM framework, 43 composite targets made up of laminates reinforced with various traditional (Carbon, Kevlar®, and E-glass) and innovative (Twaron®, Innegra®) fabrics or made up of polyethylene-based plain textiles have been tested under ballistic impact. The material properties of the fiber and the matrix were obtained from the technical sheets of the textiles provided by the producers (see Table S1 in the Supplementary Information for textile products specification). Geometrical and composition characteristics of the laminates are reported in detail in the same Table S1. Some of the fibers, bundles and related laminates (carbon of target 5, E-glass of target 4 and para-aramid of targets 8, 11–16, 21–26) were extensively characterized in a previous work by the authors [7] and found to be in very good agreement with the technical specifications in terms of both mechanical (strength, elastic modulus, failure strain) and volumetric properties (bulk density, areal density, fibers diameter). The knowledge of the technical characteristics of the textile, the geometrical characteristics of each target, and the weight of resin (whenever present) and of the textile allows to determine the fiber volume fraction of each laminate and to derive the stacking and the integration scheme to be adopted in the analytical and FEM models, respectively. The thermoset resin is for all the targets a *Bakelite® EPR L 1000 set* with density $\rho_m = 1135 kg/m^3$ and fracture strength $\sigma_m = 72.3 MPa$.

Regarding the experimental ballistic tests, each plate was lent against a block of soft wood, in order to stop the exiting projectile and measure from the depth of penetration the residual projectile velocity, knowing the perforation depth for a direct shot without interposed target. The two different tested projectiles were shot from a Trabzon gun at a distance of 5m from the targets. For this study we compare the results of a Remington 9mm FMJ Parabellum, a fragment simulating projectile (FSP 0.22in). The geometry of the analyzed projectiles is reported in Figure S2 in the Supplementary Information. A spherical steel bulk impactor of radius 5mm and mass 4.1g is also used as reference solution in the analytical model. The corresponding shape functions, calculated according to Eqs. (4), are reported in Table S2 in the Supplementary Information. The impact velocities V_0 for the projectile and the fragment are reported in Table S1 in the Supplementary Information for each of the tested cases.

3. Results and discussion

3.1. Beneficial role of compaction on impact toughness

Considering a different approach, as demonstrated in a previous work [47], upon fracture energy is dissipated in a fractal domain, whose dimension $\mathcal{D}$ is intermediate between an euclidean surface ($\mathcal{D} = 2$) and a volume ($\mathcal{D} = 3$). By extending this concept to penetrated armors, the absorbed kinetic energy by material failure is:

$W_{abs} = K_0 - K_{res} \propto w_{(D)}(\lambda A t)^{\mathcal{D}/3}$, (20) where the fractal exponent is $2 \le \mathcal{D} \le 3$, $w_{(D)}$ is the dissipated energy per fractal unit volume, and λ is the ratio between the actual damaged volume and the nominal ''impacted volume'' $At = \pi r^2 t$ (projectile imprint in case of axisymmetric geometry). In the limit case of $V_{res} = 0$ after the complete perforation of the protective layer and assuming $w_{(D)}/\rho$ as a material constant, it follows:

$$\left[1 - \zeta \frac{m v_2 \rho}{2 \rho w_{(D)}}\right]^{3/\mathcal{D}} = \lambda A t, \quad (21)$$

where $0 \le \zeta \le 1$ is the fraction of energy dissipated in the impact zone and not instantaneously propagated away by elastic and shock waves. Defining $\mathcal{M} = \rho A t$ as the penetrated material mass, it is possible to determine the critical (i.e., minimum) areal density required to stop the projectile, as a function of the material density:

$$\left[1 - \left(\frac{\mathcal{M}}{A}\right)_{crit} \frac{\zeta m v_2^2 \rho}{2 \rho w_{(D)}}\right]^{3/\mathcal{D}} = \lambda A \rho \left(\frac{\mathcal{M}}{A}\right)_{crit} = \rho t_{crit} = \zeta m v_2^2 \rho / 2 w_{(D)} \propto \rho^{1-3/\mathcal{D}}. \quad (22)$$

Since $1-3/\mathcal{D} \le 0$, the beneficial role of thickness compaction is further confirmed. We highlight that $\mathcal{D} = 3$ (i.e., $w_{(D=3)} \approx \sigma_C$, fracture strength) corresponds to $\sigma \propto t^0$ = const. (no scaling), the LEFM scaling ($\sigma \propto t^{-3/2}$) corresponds to $\mathcal{D} = 2$ with $w_{(D=2)} \approx G_C$ (fracture energy), while $\mathcal{D} = 2.5$ ($w_{(D=2.5)} \approx K_C$, fracture toughness) represents an intermediate case.

The results obtained by application of Eq. (22) are shown in Fig. 2, which reports the values of the normalized critical target mass $\mathcal{M}/A|_{crit}$ –or, equivalently, the critical target areal density– as a function of the normalized plate thickness, namely the compaction factor η. In the same figure we report the results of the analytical model incorporating LEFM (Eq. (15)), calculated for the three projectiles used in this work. The thickness compaction is predicted to affect mostly the protection against the Remington 9mm projectile, which among the three considered penetrators shows the higher relative increment in impact energy absorption due to material compaction. On the contrary, the fragment emerges to be the less sensitive to target compaction. To give an order of magnitude of the compaction effect, the fractal model (Eq. (22)) predicts that a thickness reduction of 20% ($\eta = 0.8$) by constant mass would correspond to an increase of 11.8% of the armor critical energy for $\mathcal{D} = 2.0$, +4.5% for $\mathcal{D} = 2.5$ and, obviously, no improvement for $\mathcal{D} = 3$. As expected from the assumptions, the results from the analytical model yield a scaling close to $\mathcal{D} = 2.0$. The slight discrepancy between LEFM and corresponding fractal exponent can be imputed –but not limited– to the considered strain-rate and projectile shape effects.

In order to verify the proposed fractal scaling relationship between material compaction and energy absorption capability, we evaluated via analytical calculation the critical thickness for the experimentally tested targets, that is the minimum thickness required to stop the projectile, for given properties of the single layers and the initial impact condition (projectile type and kinetic energy). Practically, we determined from Eq. (11) the minimum penetration depth which yields $V_{res} = 0$, for each of the tested plates. The results are reported in Fig. 3 and corresponding computed t_{crit} values are reported in Table S1 in the Supplementary Information. From

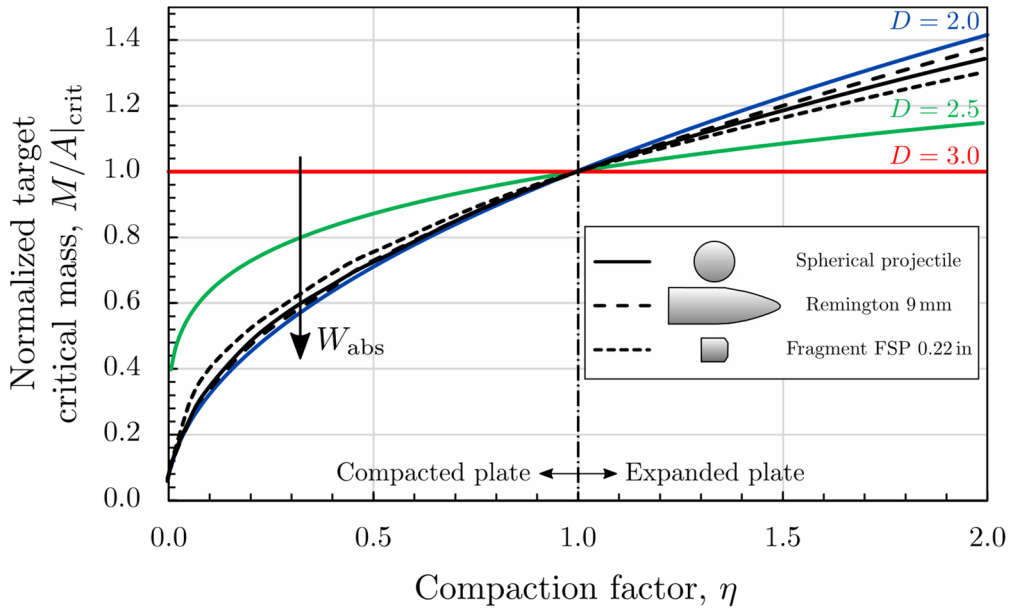

the best fit of the data we determine $\mathcal{D} \approx 2.2$ for para-aramid targets and $\mathcal{D} \approx 2.5$ for carbon based targets, while a negligible effect of compaction is observed for plain polyethylene-based textiles. The latter result can be easily explained by the absence of the resin and the quasi-incompressibility of the polyethylene textiles (Poisson's ratio equal to 0.46). The higher value of $\mathcal{D}$ for carbon composites with respect to para-aramid could confirm that these fibers are less adapt to be employed for ballistic protection as also predicted by the Cuniff criterion [6,7]. However, this could also mean that there is a lower margin for improvement due to a higher quality of carbon laminates with respect to PA ones in this study.

On the other hand, in the case of composites the formation of micro-cracks due to excessive compaction should be taken into account, especially if the pressing occurs after the partial or complete setting of the epoxy resin. This could yield to a progressive and distributed

Fig. 2. Scaling of the critical target mass (minimum mass required to stop a projectile with given projectile impact kinetic energy) as a function of the compaction factor η. The condition $\eta > 1$ indicates ideally ''expanded'' armors, as opposite to compacted ones; this condition could represent, for example, weaker samples derived from defective cleavage (cf. targets 21 and 23, Table S1 in the Supplementary Information). The fractal laws derived with the three characteristic scaling exponents (Eq. (22)) are compared with the results of the analytical model implementing LEFM (Eq. (15)), computed for the three analyzed projectiles and assuming null friction.

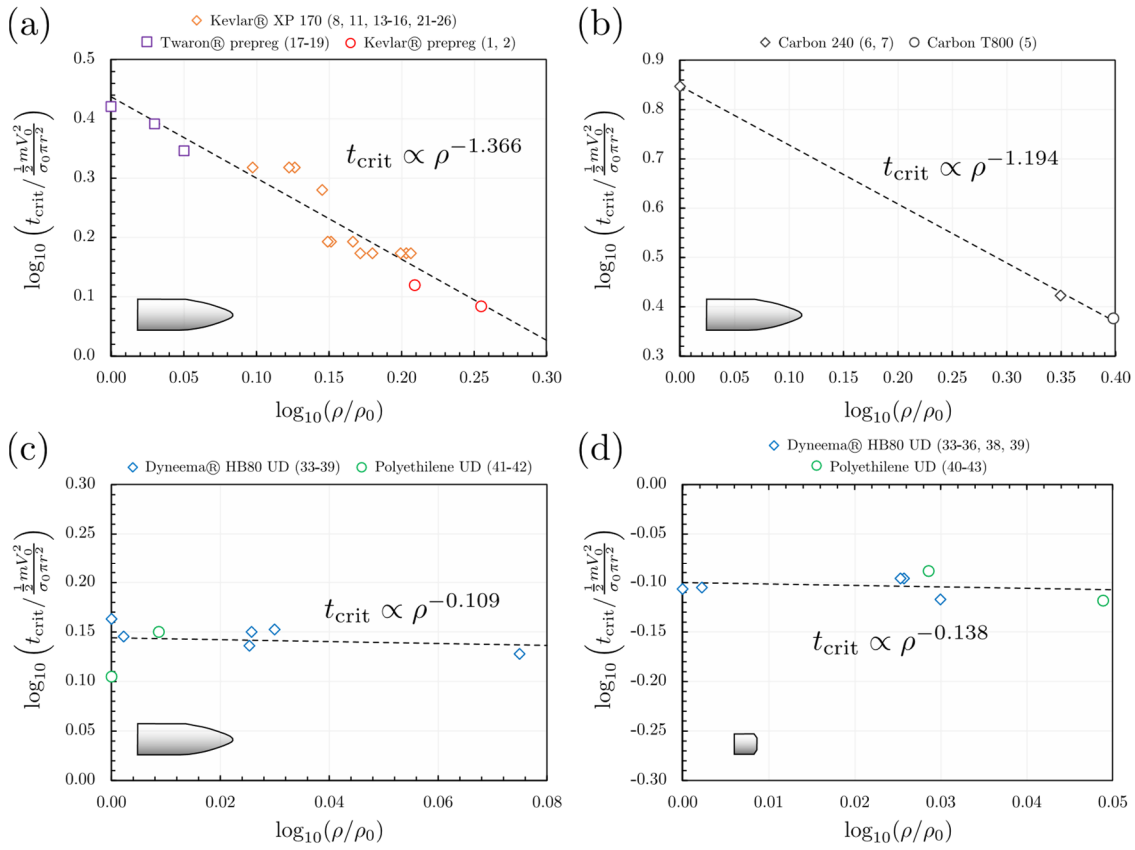

Fig. 3. Scaling of the normalized critical thickness vs. the normalized target density for: (a) Para-aramid based composites under projectile impact; (b) carbon based composites under projectile impact; (c) UD polyethylene plain textiles under projectile impact; (d) UD polyethylene plain textiles under fragment impact. The best fit exponent corresponds to $-3/D$. The critical thickness is normalized with respect to the ratio $K_0/\sigma_0\pi r^2$ in order to compare different impact scenarios (in terms of projectile kinetic energy, projectile imprint radius, and composite strength, or volume fraction) on the same graph. The density of the target is normalized with respect to ρ_0, which is the lower density among the targets of each material subgroup, assumed as the nominal uncompacted configuration. Impact conditions (in terms of velocity V_0) and other quantities are reported in Table S1 in the Supplementary Information.

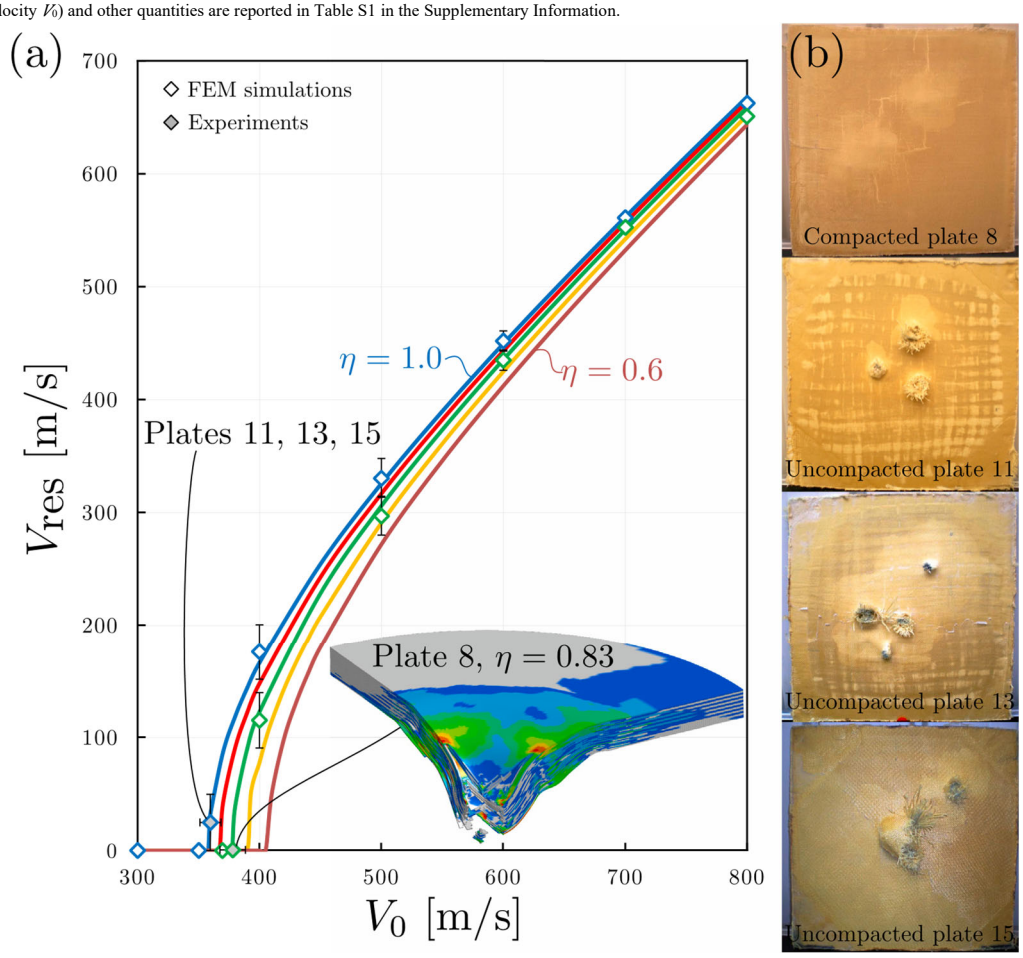

Fig. 4. (a) Analytical ballistic curves (result of Eq. (10) at different V_0) for different compaction ratio η compared with the results of finite element simulations (empty dots) and experiments (filled dots) on targets 8, 11, 13, and 15 based on para-aramid textiles. Error bars for FEM results come from the repetition of tests by accounting for the variance of the material properties of single constituents (fiber and matrix) as characterized in Ref. [7]. (b) experimental images of the rear faces of targets 8, 11, 13, and 15 (Table S1 in the Supplementary Information) after the impact of the Remington 9 mm projectile at $V_0 = 360$m/s. Simulation images for plates 11, 13, 15 are available in Ref. [7]. Experimental pictures courtesy of Vemar Helmets S.r.l., Italy.

damage and then to a decrease of the Young's modulus and strength of the matrix phase, of the matrix–fiber interface, and thus of the whole composite. This suggests to adopt, whenever possible, a cleavage pressure up to the matrix compressive strength limit, which is about 60 to 120MPa for epoxy, before material degradation. However, actual values of pressure currently used in cleavage (about 15 to 20MPa [27]) are very far from this limit and the use of higher pressures should be thoroughly investigated.

3.2. Models validation and ballistic curves

With the results in terms of projectile residual velocity obtained from the analytical and FEM models it is possible to reconstruct the ballistic curves of the targets, i.e. the $V_{res} - V_0$ plot. Assuming for the entire plate a homogeneous fracture strength $\bar{\sigma}$, the $V_{res} - V_0$ relationship assumes the following general expression resulting from energy balance, also known as Lambert–Jonas approximation [48]:

$$V_{res} = \Gamma \left(V_0^p - \frac{2\lambda\bar{\sigma}(\eta)\pi r^2 t}{m} \right)^{1/p}, \tag{23}$$

where p is generally equal to 2 for rigid projectiles, such as in our case, and Γ is a model-dependent coefficient which can be assumed equal to unity by neglecting target ejecta [49].

Fig. 4.a reports the analytically-derived ballistic curves (Eq. (10)) for the multilayers based on the *Para-aramid 170* textile (Table S1 in the Supplementary Information). It can be seen that the analytical results follow the classical form expressed by Eq. (23). By scaling the thickness, the density and the strength of the target according to LEFM, curves for different compaction factor η are obtained. Fig. 4.b reports the comparison between the plates 8, 11, 13 and 15 (see Table S1 in the Supplementary Information). Plate 8 is the only one among the considered that is not perforated despite the slightly higher impact velocity (+10m/s) with

respect to the others. With respect to target 13, target 8 has a greater compaction, i.e. $\eta = 0.83$. Plate 13 has the lowest compaction level among these four targets and it is assumed as reference uncompacted plate. Plate 11 and plate 15 have the same compaction with respect to plate 8. The best performance of target 8 with respect to 11 and 15 could be explained with the slightly greater cleavage temperature that could interact in synergy with the machine pressure to reduce defects, by enabling a more homogeneous resin flow. Additional results of numerical simulations for $\eta = 1$ and $\eta = 0.83$ at different impact velocities are reported in Fig. 4.a, showing good agreement with the scaling predicted through the analytical model.

Table S1 in the Supplementary Information reports the residual projectile/fragment velocity V_{res} recorded from experiments, finite element simulations and the prediction by our analytical model for the 43 tested targets. The results are in good agreement, despite the statistical variation of mechanical properties. This is also as a result of the quality and homogeneity of the production process and confirms that dissipation by delamination as well as by thermal effects can be considered within the limit of variance of mechanical parameters for the investigated velocity regime. A mismatch of model results, obtained

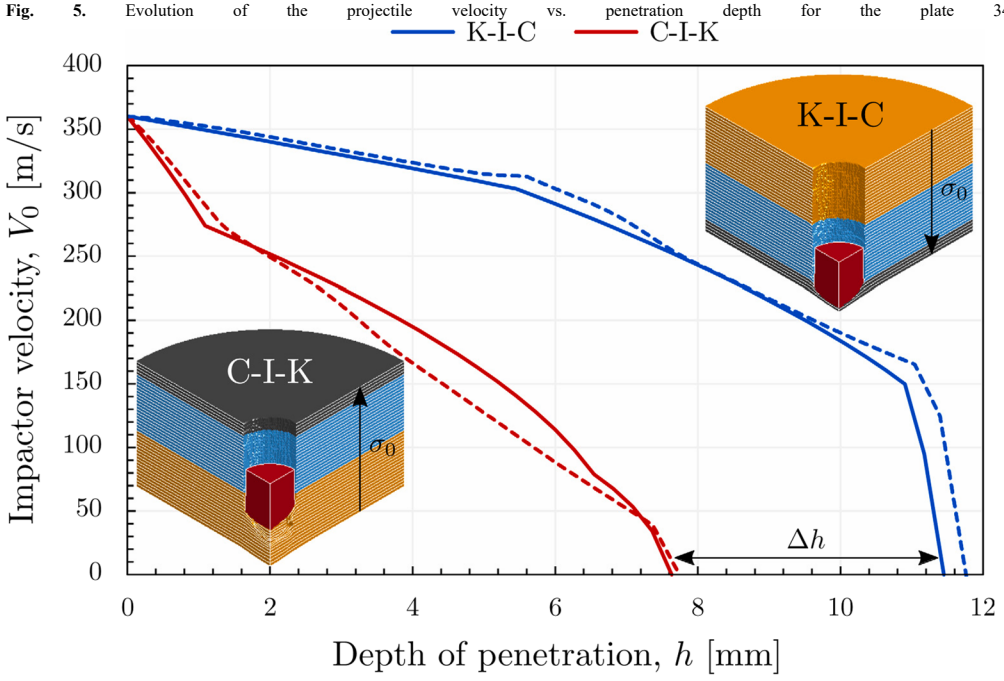

Fig. 5. Evolution of the projectile velocity vs. penetration depth for the plate 34 (heterogeneous stacking of Kevlar®, Innegra® and carbon-based composite, K-I-C, blue curves) and comparison with its symmetrical counterpart (C-I-K, red curves). A better shielding performance (i.e., in terms of energy dissipation and penetration depth) is observed when the projectile perforates materials with progressively decreasing strength. Continuous lines refer to the $v - h$ profiles computed with the analytical model, while the dashed lines depict the results of FEM simulation.

by both equations and FEM, in only two plates (nr. 21 and 23) over a total of 43 analyzed let also to identify those plates with some issues in the production process, as confirmed *a-posteriori* by the manufacturer.

The strength distribution of materials trough the armor thickness is expected to affect the energy absorption. Moreover, considering the strain-rate dependence of materials strength (Eq. (2)), the penetrator, due to its progressive deceleration, would experience a different resistant force from the same material depending on its relative position in the laminate thickness. To simplify, assuming two materials A and B with impact strength $\sigma_A > \sigma_B$, a higher energy absorption is expected for stacking sequence A→B with respect to configuration B→A. The hybrid plate 34 (see Table S1 in the Supplementary Information) can be used to test this concept, since composed by a total of 44 layers of three different materials: 20 layer of Kevlar®, 20 of Innegra®, and 4 of Carbon T300 (denoted as configuration ''K-I-C''), thus with progressively increasing nominal fracture strength σ_0, faced by the projectile. Parallel, we numerically and analytically studied the symmetrical configuration, denoted as ''C-I-K'', i.e. testing the perforation of the same armor from two opposite sides. Fig. 5 shows the evolution of the impactor velocity v vs. the instantaneous penetration depth h obtained from the analytical model and the FEM simulation for the two configurations. Both experiments and numerical simulations return a null residual velocity for the K-I-C configuration and a perforation of about 42 layers over 44, in agreement with experimental results (see Table S1 in the Supplementary Information). For the C-I-K sequence the model and the simulation both predict no perforation, but with a total penetration of 29 layers corresponding to $H_{C\text{-}I\text{-}K} \approx 7.9$mm. Therefore, a preferential order of layers is confirmed by both analytical model and FEM simulation. Moreover, the $v - h$ profiles obtained by the two different tools are in very good agreement with each other, showing that the proposed analytical model can be exploited for quick yet reliable design and verification of composite armors.

The model has also been tested for oblique impact. Fig. 6 shows the experimental results on the target 12 (para-aramid) under different angles of incidence β of the projectile, ranging from 0° to 46°. Parallel, FEM simulations with obliquity between 0° to 75° were performed. Both results are compared with the trend predicted by the analytical model. The theoretical predictions are in good agreement with both experiments and simulations over a wide range of obliquities. For incidence near to a pure tangential impact ($\beta \rightarrow 90°$) the difference between the theory and the simulated impact increases, since the real impact scenario progressively departs from model hypotheses due to incorporation and rotation of the projectile (Fig. 6). In the analyzed domain, the results are consistent with other experimental and numerical works on thin metallic targets [50], which show a significant variation on the absorbed energy with respect to the normal impact configuration starting from an obliquity greater than 45–50°.

4. Conclusions

We have developed an analytical impact model to study the ballistic properties of multilayer composite armors subjected to the impact of high-velocity projectiles. The main novelties of the proposed approach are: (i) cascade application of acknowledged penetration equations, which enables their extension to

heterogeneous multilayer targets; (ii) inclusion of the LEFM scaling of the composite material properties for the description of the effects of laminate compaction on the impact toughness; (iii) further interpretation of the latter via a fractal approach. The model provides the residual velocity of perforating projectiles or the depth of penetration in case the penetrator is fully decelerated by the target and it allows the detailed study of the projectile deceleration profile, kinetic energy dissipation, and critical armor characteristics. The analytical model has been validated via an extensive ballistic experimental campaign on multilayer composite targets and related FEM simulations. The prediction of the protection performance is quite accurate for all considered cases. The main result of the proposed model is the quantification of the beneficial effect of thickness compaction on the armor impact toughness by LEFM and fractal energy dissipation models. This suggests interesting implications for the role of the production procedures on the protection capability, which need to be thoroughly investigated. The developed tools can be employed in the design and optimization of composite armors under different impact scenarios and employing a large variety of reinforcing fibers, including novel nanomaterials.

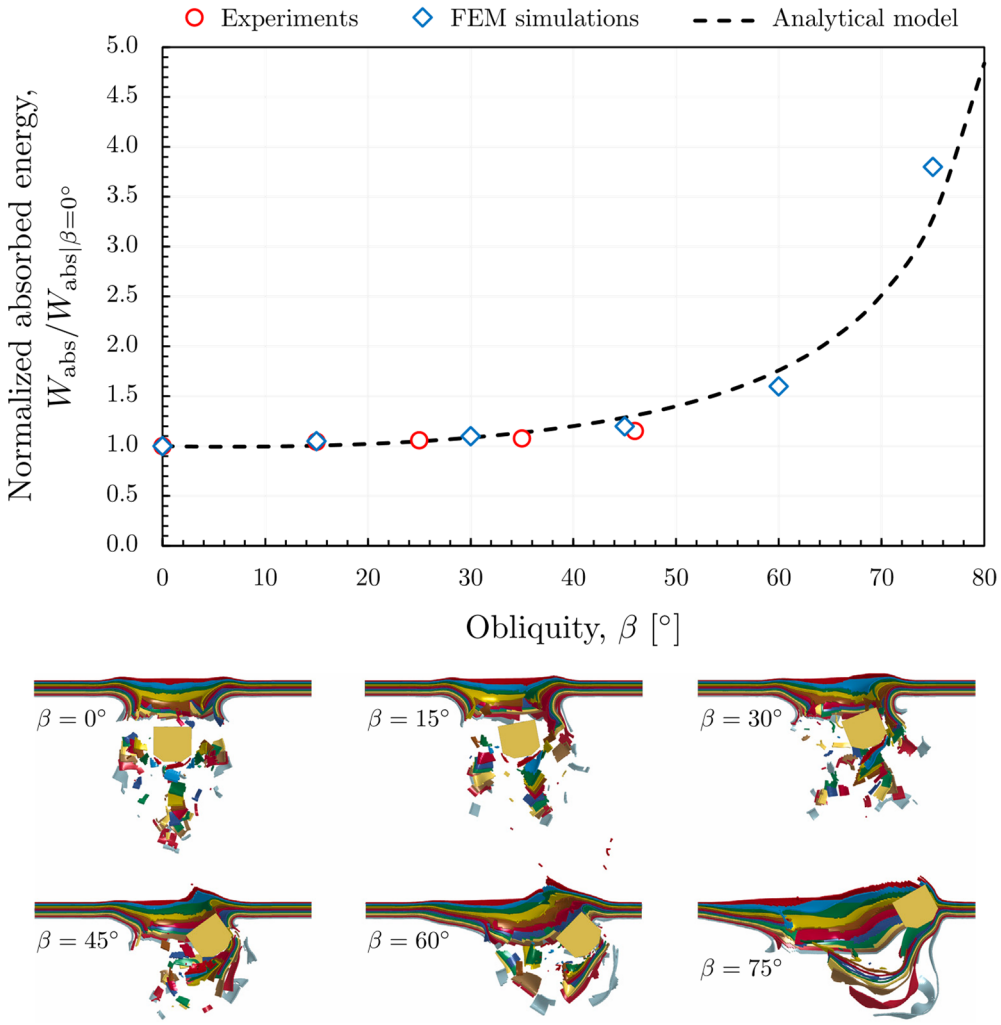

Fig. 6. Absorbed energy (W_{abs}) as a function of the impact angle, normalized with respect to the reference normal impact configuration ($\beta = 0°$). Experimental data up to obliquity of 46° are complemented with FEM simulations up to $\beta = 75°$ and compared with the prediction of the analytical model developed in this work (dashed curve). The analysis refers to plate 5 impacted at $V_0 = 360$ m/s by FSP fragment. A visualization of the plate perforation obtained from simulations for different obliquities is depicted in the bottom panel.

CRediT authorship contribution statement

Stefano Signetti: Conceptualization, Methodology, Software, Validation, Formal analysis, Investigation, Data curation, Writing – original draft, Writing – review & editing, Visualization. **Seunghwa Ryu:** Formal analysis, Writing – review & editing. **Nicola M. Pugno:** Conceptualization, Methodology, Formal analysis, Writing – review & editing, Supervision, Funding acquisition.

Declaration of competing interest

The authors declare that they have no known competing financial interests or personal relationships that could have appeared to influence the work reported in this paper.

Data availability

The raw/processed data required to reproduce these findings are available as Supplementary Material and in Ref. [7].

Acknowledgments

SS thanks AMET s.r.l. (Torino, Italy), in the persons of the Technical Director Paolo Cavallo and of the former CAE Department Director Michele Rabito Crescimanno, for the kind collaboration and support within the Alta Scuola Politecnica Project ‘‘Spider Silk - Inspired SuperTough Nanoarmors’’, especially for their introduction in advanced nonlinear FEM modeling. NMP is supported by the European Commission under the FET Open ‘‘Boheme’’ grant no. 863179. SHR is supported by the Basic Science Research Program (2022R1A2B5B02002365) funded by the National Research Foundation of Korea (NRF).

References

[1] US Department of Justice. Ballistic resistance of body armor - NIJ standard-0101.06. 2008.
[2] Boslough MB, Ang JA, Chhabildas LC, Reinhart WD, Hall CA, Cour-Palais BG, et al. Hypervelocity testing of advanced shielding concepts for spacecraft against impacts to 10 km/s. Int J Impact Eng 1993;14(1–4):95–106. http://dx.doi.org/ 10.1016/0734-743X(93)90012-V.
[3] Signetti S, Nicotra M, Colonna M, Pugno NM. Modeling and simulation of the impact behavior of soft polymeric-foam-based back protectors for winter sports. J Sci Med Sport 2019;22(S1). S65–S70. http://dx.doi.org/10.1016/j.jsams.2018.
10.007.
[4] Cantwell WJ, Morton J. The impact resistance of composite materials - A review. Composites 1991;22(5):347–62. http://dx.doi.org/10.1016/0010-4361(91) 90549-V.
[5] Hoog PJ. Composites in Armor. Science 2006;314(5802):1100–1. http://dx.doi. org/10.1126/science.1131118.
[6] Cuniff PM. Dimensionless parameters for optimization of textile-based body armor systems. In: Proceedings of the 18th International Symposium of Ballistics, 1999, p. 1303–10.
[7] Signetti S, Bosia F, Ryu S, Pugno NM. An experimental/numerical study on the scaling of impact strength and toughness in composite laminates for ballistic applications. Compos Part B-Eng 2020;196:108090. http://dx.doi.org/10.1016/j. compositesb.2020.108090.
[8] Kumar BG, Singh RP, Nakamura T. Degradation of carbon fiber-reinforced epoxy composites by ultraviolet radiation and condensation. J Compos Mater 2002;36(24):2713–33. http://dx.doi.org/10.1177/002199802761675511.
[9] Harris B. Engineering composite materials. 2nd ed.. London: Institute of Materials; 1999.
[10] Ganczakowski HL, Beaumont PWR. The behaviour of Kevlar fibre-epoxy laminates under static and fatigue loadings. Part I — experimental. Compos Sci Tech 1989;36(4):299–319. http://dx.doi.org/10.1016/0266-3538(89)90044-4.
[11] Cheeseman BA, Bogetti TA. Ballistic impact into fabric and compliant composite laminates. Compos Struct 2003;61(1–2):161–73. http://dx.doi.org/10.1016/ S0263-8223(03)00029-1.
[12] Signetti S, Pugno NM. Evidence of optimal interfaces in bio-inspired ceramic-composite panels for superior ballistic protection. J Eur Ceram Soc 2014;34(11):2823–31. http://dx.doi.org/10.1016/j.jeurceramsoc.2013.12.039.
[13] Zinszner JL, Forquin P, Rossiquet G. Experimental and numerical analysis of the dynamic fragmentation in a SiC ceramic under impact. Int J Impact Eng
2015;76:9–19. http://dx.doi.org/10.1016/j.ijimpeng.2014.07.007.
[14] LaSalvia JC, Gyekenyesi AL, Halbig M, editors. Advances in ceramic Armor X. In: Ceramic Engineering and Science Proceedings, Vol. 35, (4). John Wiley & Sons; 2014, URL: http://eu.wiley.com/WileyCDA/WileyTitle/productCd-1119040604. html.
[15] Liu W, Chen Z, Chen Z, Cheng X, Wang Y, Chen X, et al. Influence of different back laminate layers on ballistic performance of ceramic composite armor. Mater Design 2015;87:421–7. http://dx.doi.org/10.1016/j.matdes.2015.08.024.
[16] Bruet BJF, Song J, Boyce MC, Ortiz C. Materials design principles of ancient fish armour. Nat Mater 2008;7(9):748–56. http://dx.doi.org/10.1038/nmat2231.
[17] Yang W, Chen IH, Gludovatz B, Zimmermann EA, Ritchie RO, Meyers MA. Natural Flexible Dermal Armour. Adv Mater 2013;25(1):31–48. http://dx.doi. org/10.1002/adma.201202713.
[18] Yang W, Sherman VR, Gludovatz B, Mackey M, Zimmermann EA, Chang EH, et al. Protective role of Arapaima gigas fish scales: Structure and mechanical behavior. Acta Biomater 2014;10(8):3599–614. http://dx.doi.org/10.1016/j.actbio. 2014.04.009.
[19] Backman ME, Goldsmith W. The mechanics of penetration of projectile into targets. Int J Eng Sci 1978;16(1):1–99. http://dx.doi.org/10.1016/0020-7225(78) 90002-2.
[20] Guoqi Z, Goldsmith W, Dharan CKH. Penetration of laminated Kevlar by projectiles-II. Analytical model. Int J Solids Struct 1992;29(4):421–36. http: //dx.doi.org/10.1016/0020-7683(92)90208-B.
[21] Parga-Landa B, Hernández-Olivares F. An analytical model to predict impact behaviour of soft armours. Int J Impact Eng 1995;16(3):455–66. http://dx.doi. org/10.1016/0734-743X(94)00054-Z.
[22] Phoenix SL, Porwal PK. A new membrane model for the ballistic impact response and V_{50} performance of multi-ply fibrous systems. Int J Solids Struct 2003;40(24):6723–65. http://dx.doi.org/10.1016/S0020-7683(03)00329-9.
[23] Gu B. Analytical modeling for the ballistic perforation of planar plain-woven fabric target by projectile. Compos B-Eng 2003;34(4):361–71. http://dx.doi.org/ 10.1016/S1359-8368(02)00137-3.
[24] Porwal PK, Phoenix SL. Modeling system effects in ballistic impact into multi-layered fibrous materials for soft body armor. Int J Fracture 2005;135(1–4):217–49. http://dx.doi.org/10.1007/s10704-005-3993-9.
[25] López-Puente J, Zaera R, Navarro C. An analytical model for high velocity impacts on thin CFRPs woven laminated plates. Int J Solids Struct
2007;44(9):2837–51. http://dx.doi.org/10.1016/j.ijsolstr.2006.08.022.
[26] Mamivand M, Liaghat GH. A model for ballistic impact on multi-layer fabric targets. Int J Impact Eng 2010;37(7):806–12. http://dx.doi.org/10.1016/j.ijimpeng.
2010.01.003.
[27] Hubert P, Pousartip A. Aspects of the compaction of composite angle laminates: An experimental investigation. J Compos Mater 2001;35(1):2–26. http://dx.doi.org/10.1177/002199801772661849.
[28] Jacobs MJN, van Dingenen JLJ. Ballistic protection mechanisms in personal armour. J Mater Sci 2001;36(13):3137–42. http://dx.doi.org/10.1023/A: 1017922000090.
[29] Lim CT, Shim VPW, Ng YH. Finite-element modeling of the ballistic impact of fabric armor. Int J Impact Eng 2003;28(1):13–31. http://dx.doi.org/10.1016/ S0734-743X(02)00031-3.
[30] Gama BA, Gillespie JW. Finite element modeling of impact, damage evolution and penetration of thick-section composites. Int J Impact Eng 2011;38(4):181–97. http://dx.doi.org/10.1016/j.ijimpeng.2010.11.001.
[31] Signetti S, Taioli S, Pugno NM. 2D material armors showing superior impact strength of few layers. ACS Appl Mater Inter 2017;9(46):40820–30. http://dx. doi.org/10.1021/acsami.7b12030.
[32] Goldsmith W. Non-ideal projectile impact on targets. Int J Impact Eng
1999;22(2–3):95–395. http://dx.doi.org/10.1016/S0734-743X(98)00031-1.
[33] Alil L-C, Arrigoni M, Badea S, Ginghină R, Matache L-C, Mostovykh P. Ballistic study of Tensylon®–based panels. Express Polym Lett 2018;12(6):491–504. http: //dx.doi.org/10.3144/expresspolymlett.2018.42.
[34] Banichuk NV, Ivanova SY, Makeev EV. On the penetration of nonaxisymmetric bodies into a deformable solid medium and their shape optimization. Mech Sol 2008;43(4):671–7. http://dx.doi.org/10.3103/S0025654408040158.
[35] Forrestal MJ, Tzou DY. A spherical cavity-expansion penetration model for concrete targets. Int J Solids Struct 1997;34(31–32):4127–46. http://dx.doi.org/ 10.1016/S0020-7683(97)00017-6.
[36] Ben-Dor G, Dubinsky A, Elperin T. High-speed penetration modeling and shape optimization of the projectile penetrating into concrete shields. Mech Based Des Struc 2009;37(4):538–49. http://dx.doi.org/10.1080/15397730903272830.
[37] Forrestal MJ, Altman BS, Cargile JD, Hanchak SJ. An empirical equation for penetration depth of ogive-nose projectiles into concrete targets. Int J Impact Eng 1994;15(4):395–405. http://dx.doi.org/10.1016/0734-743X(94)80024-4.
[38] Abrate S. Ballistic impact on composites. In: Proceedings of the 16th International Conference on Composite Materials. 2007.
[39] Ashby MF. Materials selection in mechanical design. 3rd ed.. Burlington: Butterworth-Heinemann; 1999.
[40] Griffith AA. The phenomena of rupture and flow in solids. Philos T R Soc A
1921;221:582–93. http://dx.doi.org/10.1098/rsta.1921.0006.

[41] Hallquist JO. LS-DYNA theory manual. Livermore: Livermore Software Technology Corporation; 2006.
[42] Liu WK, Guo Y, Tang S, Belytschko T. A multiple-quadrature eight-node hexahedral finite element for large deformation elastoplastic analysis. Comput Method Appl M 1998;154(1):69–132. http://dx.doi.org/10.1016/S0045-7825(97)001060.
[43] Chen WT, Engel PA. Impact and contact stress analysis in multilayer media. Int J Solids Struct 1972;8(11):1257–81. http://dx.doi.org/10.1016/0020-7683(72) 90079-0.
[44] Belytschko T, Ong JSJ, Liu WK, Kennedy JM. Hourglass control in linear and nonlinear problems. Comput Method Appl M 1984;43(3):69–132. http://dx.doi. org/10.1016/0045-7825(84)90067-7.
[45] Matzenmiller A, Lubliner J, Taylor RL. A constitutive model for anisotropic damage in fiber-composites. Mech Mater 1995;20(2):125–52. http://dx.doi.org/ 10.1016/0167-6636(94)00053-0.
[46] Lopes C, Gurdal Z, Camanho P, Maimi P, Gonzalez E. Simulation of lowvelocity impact damage on composite laminates. In: Proceedings of the 50th AIAA/ASME/ASCE/AHS/ASC structures, structural dynamics, and materials conference. 2009, p. 2445. http://dx.doi.org/10.2514/6.2009-2445.
[47] Carpinteri A, Pugno NM. Are scaling laws on strength of solids related to mechanics or to geometry?. Nat Mater 2005;43:421–3. http://dx.doi.org/10. 1038/nmat1408.
[48] Lambert JP, Jonas GH. Towards standardization in terminal ballistics testing: velocity representation. Technical Report BRL-R-1852, Aberdeen, MD, USA: Army Ballistic Research Laboratory; 1976.
[49] Recht RF, Ipson TW. Ballistic perforation dynamics. J Appl Mech 1963;30(3):384–90. http://dx.doi.org/10.1115/1.3636566.
[50] Iqbal MA, Diwakar A, Rajput A, Gupta NK. Influence of projectile shape and incidence angle on the ballistic limit and failure mechanism of thick steel plates. Theor Appl Fract Mech 2012;62:40–53. http://dx.doi.org/10.1016/j.tafmec.2013.
01.005.

Impact mechanics of multilayer composite armors: analytical modeling, FEM numerical simulation, and ballistic experiments

- Supplementary Information -

Stefano Signetti,*,† Seunghwa Ryu,‡ and Nicola Pugno*,†,¶

†*Laboratory of Bioinspired, Bionic, Nano, Meta Materials & Mechanics,*

Department of Civil, Environmental and Mechanical Engineering,

University of Trento, I-38123 Trento, Italy

‡*Department of Mechanical Engineering, Korea Advanced Institute of Science and Technology (KAIST), 291 Daehak-ro, Yuseong-gu, Daejeon 34141, Republic of Korea*

¶*School of Engineering and Materials Science,*

Queen Mary University of London, London E1 4NS, UK

E-mail: stefano.signetti@ex-staff.unitn.it; nicola.pugno@unitn.it

S1 **Finite element model**

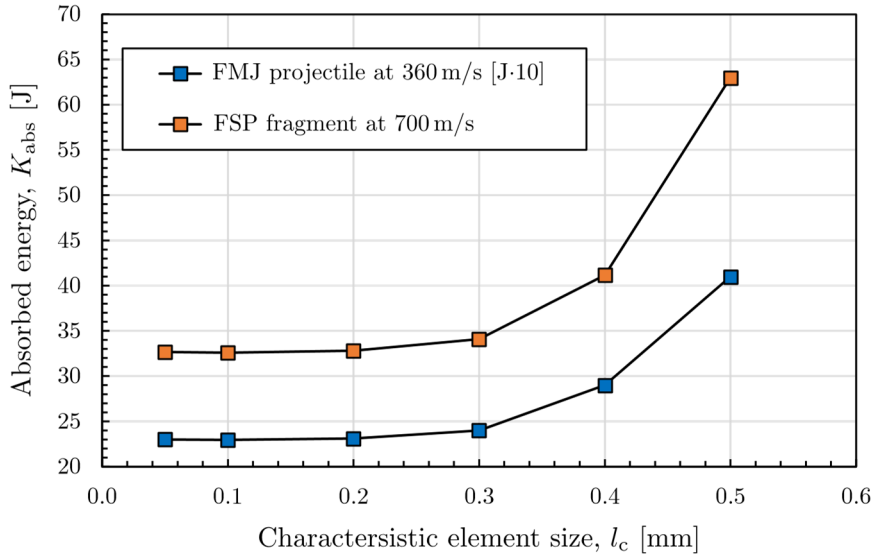

Figure S1: Convergence test on the absorbed energy by the target as a function of the thick shell element in-plane edge size executed for 1 layer of material of plate 8 (see Table S1). Below the impact area the thick shell elements have aspect ratio 1:1 with l_c = 0.1mm.

Table S1

S2 Target materials and comparison between theory, simulations and impact experiments

In the following we report the geometrical and composition characteristics of the 43 tested plates together with the results of ballistic tests, in terms of projectile/fragment residual velocity, compared to analytical model and simulation.

S2

	Target geometry			Laminate composition				Cleavage parameters			Projectile impact test				Fragment impact test				
Textile type	$b \cdot l$ [mm^2]	t [mm]	n	ρ [kg/m^3]	W_{epoxy} [g]	W_{textile} [g]	ρ_{textile} [kg/m^3]	p [bar]	T [°C]	time [min]	V_0 [m/s]	$V_{\text{res,exp}}$ [m/s]	$V_{\text{res,an}}$ [m/s]	$V_{\text{res,sim}}$ [m/s]	V_0 [m/s]	$V_{\text{res,exp}}$ [m/s]	$V_{\text{res,an}}$ [m/s]	$V_{\text{res,sim}}$ [m/s]	t_{crit} [mm]
uPont Kevlar XP prepreg	370x370	3	17	1826	n.a.	n.a.	n.a.	80	130	10	360	110	120	117	-	-	-	-	3.5
uPont Kevlar XP prepreg	370x370	2	10	1644	n.a.	n.a.	n.a.	80	130	10	360	221	233	224	-	-	-	-	3.8
SAATI Kevlar KQX 240	370x370	6	21	1290	350	710	247	30	80	20	360	55	57	58	-	-	-	-	6.3
Glass Angeloni VV - 300P	370x370	3	16	2277	130	690	315	80	80	20	360	110	126	115	-	-	-	-	3.6
arbon Angeloni GG 301 T8	370x370	4	17	2009	180	745	320	80	80	20	360	110	106	103	-	-	-	-	4.7
arbon Angeloni GG 240 T	370x370	4	21	1797	180	690	240	80	80	20	360	166	205	161	-	-	-	-	5.1
arbon Angeloni GG 240 T	370x370	10	21	804	250	690	240	0	0	0	360	193	194	203	-	-	-	-	16.2
Angeloni aramid style 170	370x370	5	30	1490	370	698	170	80	80	20	370	0	0	0	-	-	-	-	4.5
SAATI Kevlar KQX 240	370x370	4	21	2009	350	710	247	80	80	20	360	138	110	121	-	-	-	-	4.8
NCERT polyethylene tissue	370x370	7	9	1054	250	1010	950	80	80	20	360	0	0	0	-	-	-	-	4.7
Angeloni aramid style 170	370x370	5	30	1439	280	698	170	80	75	20	360	27	0	3	-	-	-	-	4.5
Angeloni aramid style 170	370x370	10	30	877	360	698	170	80	75	20	360	0	0	0	-	-	-	-	9.7
Angeloni aramid style 170	370x370	7	30	1419	410	698	170	80	75	20	360	27	61	34	-	-	-	-	5.5
Angeloni aramid style 170	370x370	5	30	1607	230	698	170	80	75	20	360	27	0	0	-	-	-	-	4.3
Angeloni aramid style 170	370x370	5	30	1508	370	698	170	80	75	20	360	27	0	0	-	-	-	-	4.3
Angeloni aramid style 170	370x370	5	30	1432	210	698	170	80	75	20	360	0	0	0	-	-	-	-	4.5
Teinjin prepreg twaron	400x400	4	10	1141	n.a.	n.a.	n.a.	60	170	15	360	0	0	0	-	-	-	-	6.4
Teinjin prepreg twaron	400x400	5	12	1088	n.a.	n.a.	n.a.	60	170	15	360	0	0	0	-	-	-	-	7.1
Teinjin prepreg twaron	400x400	8	18	1016	n.a.	n.a.	n.a.	60	170	15	360	0	0	0	-	-	-	-	7.6
Montefibre fidion	400x400	8	10	629	0	687	629	100	100	3	360	0	0	0	-	-	-	-	8.0
Angeloni aramid style 170	370x370	5	25	1271	220	582	170	80	80	20	360	0	126	103	-	-	-	-	6.0
Angeloni aramid style 170	370x370	5	30	1622	435	698	170	80	80	15	360	0	0	0	-	-	-	-	4.3
Angeloni aramid style 170	370x370	4	20	1359	220	465	170	80	80	20	360	27	182	150	-	-	-	-	6.0
Angeloni aramid style 170	370x370	5	30	1537	270	698	170	60	80	20	360	0	0	0	-	-	-	-	4.3
Angeloni aramid style 170	370x370	5	30	1633	330	698	170	40	80	20	360	0	0	0	-	-	-	-	4.3
Angeloni aramid style 170	370x370	6	30	1346	325	698	170	20	80	20	360	0	0	0	-	-	-	-	6.0
Polyetilene AB26-UD	176x188	3	20	1854	0	175	264	0	0	0	360	0	0	0	-	-	-	-	2.7
Dyneema HB80 UD	170x170	6	10	531	0	42	145	0	0	0	360	0	0	0	-	-	-	-	5.4
Lenzi Egisto Dynafelt 400	370x370	8	12	968	390	670	408	100	75	20	360	27	57	44	-	-	-	-	8.7
Lenzi Egisto Innegra	370x370	7	18	981	200	678	275	80	75	20	360	27	39	42	-	-	-	-	7.4
Polyetilene UD fabric	200x400	8	40	883	0	528	165	80	75	20	360	0	0	0	-	-	-	-	3.1
UD Kevlar fabric	200x400	7	60	955	0	1056	220	80	75	20	360	0	0	0	-	-	-	-	4.0
Dyneema HB80 UD	400x400	6	43	1025	0	998	145	150	100	20	360	0	0	0	710	PP	0	0	5.2/4.3
Angeloni aramid style 170 Lenzi Egisto Innegra arbon Angeloni GG 301 T8	370x370	3 8 1	20 20 4	1029	296	1394 (tot.)	170 275 320	100	80	20	388	0	0	0	-	-	-	-	8.0
Dyneema HB80 UD	400x400	6	43	1024	0	1011	147	150	100	20	393	0	0	0	710	PP	0	0	6.0/4.3
Dyneema HB80 UD	400x400	7	47	971	0	1105	147	170	110	25	392	0	0	0	804	PP	0	0	6.1/5.4
Dyneema HB80 UD	370x370	7	45	1148	0	906	147	100	0	10	390	0	0	0	-	-	-	-	5.8
Dyneema HB80 UD	400x400	8	56	1035	0	1317	147	150	100	20	352	0	0	0	850	PP	0	0	5.0/5.9
Dyneema HB80 UD	400x400	9	59	966	0	1388	147	170	110	25	358	0	0	0	870	PP	0	0	6.3
Polyetilene UD Fabric	370x370	8	50	1004	0	1129	165	100	55	45	-	-	-	-	720	CP	0	0	4.5
Polyetilene UD Fabric	370x370	8	45	940	0	1016	165	155	55	45	390	0	0	0	-	-	-	-	5.5
Polyetilene UD Fabric	370x370	8	45	959	0	1016	165	155	55	45	360	0	0	0	-	-	-	-	5.2
Polyetilene UD Fabric	370x370	7	45	1052	0	1016	165	100	55	50	-	-	-	-	720	CP	0	0	4.2

. Summary of characteristics and impact results for the 43 tested composite targets. For each sample are reported: the textile type according to the producers specifications, the geometry of the target (in-plane dimensions b ckness t, and number of layers n), the plate composition (the density ρ of the target and textiles, the weight W of the epoxy and textiles), and the production process parameters used for cleavage and curing (pressure p, ure T, and time). The fibre volume fraction was determined *a posteriori* from the geometry of targets and the respective weights of resin (Bakelite® EPR L 1000 set with density 1135 kg/m^3 and 72.3 MPa of tensile strength) es. For each target are then reported the initial impact velocity of either projectile and/or fragment and the respective residual velocity $V_{\text{res,exp}}$ as measured in experiments and computed by the analytical model and FEM ns ($V_{\text{res,an}}$ and $V_{\text{res,sim}}$, respectively). For the fragment, PP identifies a partial perforation of the target while CP means a complete perforation ($H \equiv$ t). The critical thickness t_{crit}, i.e. the minimum thickness required to stop tile/fragment as determined from the analytical model, is reported in the last column. Samples' geometry, composition, cleavage parameters, and experimental impact data courtesy of Vemar Helmets s.r.l..

S3 **Geometrical characteristics of the tested projectiles**

In general, the integrals of Equations (4) in the main text have to be solved numerically for profiles described by high-degree functions. A piecewise solution could be also necessary, either due to peculiar projectile profile or the current depth of perforation h_i in each layer (Figure 1 in the main text), which affect the integration domain. In the case of a spherical projectile in a bulk material, the integrals result into the following closed-form expressions, by assuming

$\sqrt{r^2 - (x - r)^2}$ within the domain $x \in [0;r]$ (after transforming in polar the profile curve $y = r$

coordinates for convenience):

$$J_0 = \frac{\pi}{4}\mu r^2, \tag{S1}$$

$$J_1 = \left(\frac{1}{6} - \frac{\mu}{3}\right) r^2, \tag{S2}$$

$$J_2 = \left(\frac{1}{4} - \frac{\pi}{16}\mu\right) r^2. \tag{S3}$$

Note that the above relationships, as well as Equations (4) in the main text in general, yield to the same result for hollow and filled projectiles of equal external profile, since these functions account only for the role of the projectile geometry, assumed to be rigid. The profile functions and corresponding integration domains for the three projectiles analyzed in this work are reported in Table S2 (see Figure S2 for the projectile and fragment geometries).

Table S2: Geometrical (shape function and domain) and mass characteristics of the three studied projectiles.

Projectile type	Function [mm]	Domain [mm]	m [g]	r [mm]
Spherical	$y = \sqrt{r^2 - (x - r)^2}$	$x \in [0;r]$	4.110	5.000
FMJ 9mm	$y = 2.2816x^{0.3033}$	$x \in [0;10.54]$	8.040	4.515
FSP 0.22in	$y = 1.428x + 1.270$	$x \in [0;1.02]$	1.102	2.731

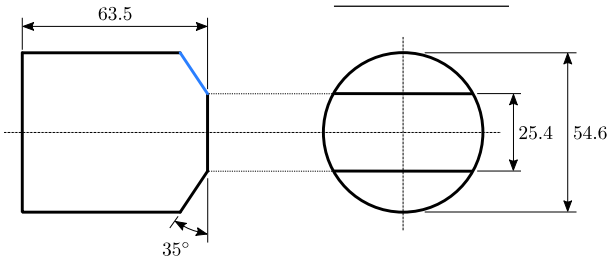

(a)

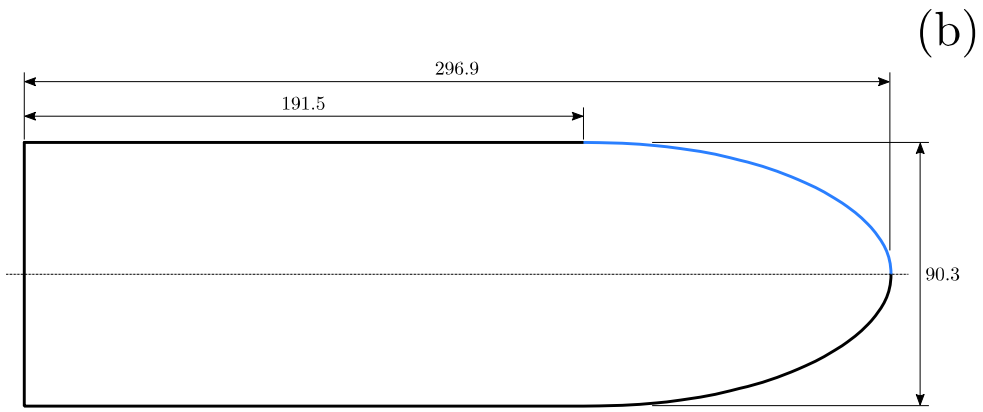

Figure S2: Geometrical dimensions employed in the analytical and FEM models of (a) fragment simulating projectile (FSP) caliber 0.22inches[1] and (b) Remington 9mm FMJ.[2] The blue lines highlight the profiles described by the respective functions in Table S2.

References

(1) *MIL-DTL-46593B - DETAIL SPECIFICATION PROJECTILE, CALIBERS .22, .30, .50, AND 20MM FRAGMENT-SIMULATING*; U.S. Army Research Laboratory, 2006.

(2) *MAS/132-MMS/4090 - STANAG 4090 LAND (Edition 2) SMALL ARMS AMMUNITION (9 mm PARABELLUM)*; NATO Military Agency for Standardization, 1982.